MEASURING BREAKING WAVE HEIGHTS USING VIDEO

A THESIS SUBMITTED TO

THE GLOBAL ENVIORNMENTAL SCIENCE
UNDERGRADUATE DIVISION OF
THE UNIVERSITY OF HAWAI'I AT MANOA

IN PARTIAL FULFULLMENT
OF THE REQUIREMENTS FOR THE DEGREE OF

BACHELOR OF SCIENCE
IN
GLOBAL ENVIRONMENTAL SCIENCE

DECEMBER, 2005

Tyson Hilmer

Thesis Advisor:

Dr. Mark Merrifield

I certify that I have read this thesis and that, in my opinion, it is satisfactory in scope and quality as a thesis for the degree of Bachelor of Science in Global Environmental Science.

THESIS ADVISOR

Dr. Mark Merrifield
Department of Oceanography

ABSTRACT

The dominant process for the transfer of mass and energy into the surf zone is wave breaking. Typhoons and heavy storms create extreme conditions wherein storm surge, coastal setup, and large swell combine to cause flooding and direct damage to coastal infrastructure via wave energy. The majority of research in the nearshore has been conducted under moderate conditions, presumably due to the logistical difficulties of maintaining instrumentation under storm conditions, as well as the infrequency of such events. This paper describes in detail a method for remotely measuring breaking wave heights over a range of environmental conditions using video, and its on-going application in a high-energy nearshore environment.

A 640x480 pixel analog surveillance camera, with a view of approximately 0.04 km^2 and a mean horizontal resolution of 0.5 m, was affixed to a rigid structure overlooking a uniform shallow reef near Ipan, Guam. Image data were collected at 2 Hz along a shore-normal transect continuously for three months. Broken wave heights, offshore and secondary swell wavelengths and velocities, and wave refractions are successfully resolved using this technique. A novel feature-detection algorithm was developed for accurately and autonomously generating a time series of broken wave heights. Initial comparisons between video measurements of breaking wave height show a strong correspondence with *in-situ* pressure sensor data.

TABLE OF CONTENTS

LIST OF FIGURES

Figure **Page**

Introduction

The nearshore is an energetic region where the dynamics of fluid motions become increasingly complex due to interactions with the underlying bathymetry. Waves propagating from deeper water interact with the bottom profile, causing them to shoal and eventually break. The dominant process for the transfer of mass and energy into the surf zone is wave breaking. After a wave has broken, the flux of mass and energy continues in the form of a bore traveling over shallow water, eventually collapsing on shore as swash. Throughout this process wave energy is shifted to higher frequencies and dissipated as motions become increasingly turbulent.

Breaking waves can be characterized into four classes based on how rapidly the waveform is degraded, i.e. how quickly the wave energy is attenuated (Galvin, 1968, quoted from Smith 2002). The four categories are; surging, collapsing, spilling, and plunging breakers. For surging and collapsing breakers, the crest remains unbroken while the shoreward wave face breaks slightly. Spilling breakers maintain a general waveform while the wave crest spills down the face of the wave. Plunging breakers are the most energetic; with the wave crest and face completely collapsing and plunging into the trough.

Typhoons and heavy storms create extreme conditions for the transfer of mass and energy in the nearshore and coastal region. Storm surge, coastal setup, and large swell combine to cause flooding and direct damage to coastal infrastructure via wave energy (Smith, 2002). Storm surge is an elevation of sea surface height due to decreased atmospheric pressure and increased wind stress commonly associated with storms. Coastal, or wave, setup is an additional elevation of sea surface height due to the mass transfer of water into the nearshore driven by wave breaking. Both of the aforementioned sea surface elevation processes exacerbate the damaging effects of increased wave energy during storm events by allowing waves to propagate further inshore before breaking, and thus allow greater destructive forces to be transmitted to the shoreline and nearby structures.

The ability to measure and predict wave transformation, water levels, and nearshore currents under extreme energy conditions is required before potential damages from such events can be assessed and planned for. Ultimately, our predictive ability is dependent on how well these physical processes are understood. The majority of research in the nearshore has been conducted under moderate conditions, presumably due to the logistical difficulties of maintaining instrumentation under destructive conditions, as well as the infrequency of such events. Ahrens et al. (1993) notes a lack of data for run-up under severe conditions. Yet, it is the under-sampled extreme events that pose the greatest threat to our coastal communities.

This paper describes in detail a method for measuring breaking wave heights using video across a range of environmental conditions, and its on-going application in a high-energy nearshore environment. A non-comprehensive review of previous studies employing video in the nearshore is given in Section 1. A brief technical description of video instrumentation, and a discussion of logistical considerations for using video are given in Sections 2 and 3, respectively. Section 4 explains the methodology by which a timeseries of breaking wave heights can be obtained from video sampling. Initial results from this on-going study are given in Section 5, with a summary discussion in Section 6.

1. Previous Studies

Traditional field studies in the nearshore have employed a variety of instruments for measuring fluid motions. Velocities are measured using ducted impeller current meters (DICM), electro-magnetic current meters (EMCM), and acoustic Doppler current profilers (ADCP). Pressure sensors mounted to the seafloor are used to record wave length and period. Wave gauges measure wave height. Bathymetry surveys are accomplished using a survey rod in shallow depths in conjunction with boat fathometers (Stockdon & Holman, 2000). Dual resistance wires and buried pressure sensors have been used for measuring run-up (Holman & Guza, 1984)

More recently, video imagery has been used to measure nearshore processes. Lippman and Holman (1989, 1990) used video for measuring the spatial and temporal variability of submerged sand bars. Konicki and Holman (2000) resolved transverse sand bars previously undetected from bathymetric surveys. Wave run-up (Holland & Holman, 1999; Bailey & Shand, 1994, Aagaard & Holm, 1989) and beach slope morphology (Plant & Holman, 1997) have also been quantified. Stockdon and Holman (2000) used a grid of image pixels to measure wave celerities and determine a full bathymetry profile for the region sampled. Video techniques have also been evaluated in comparison to traditional instrumentation. Lippmann and Holman (1991) compared estimates of phase speed, period, and direction measured from image pixel intensities to in-situ pressure sensors and found high cross-spectral correlations. Puleo et al. (2003) compared measurements of surf zone and swash velocities between radar and video. Full horizontal velocity fields for swash motions (Holland et al., 2001) have been generated using a video technique entitled particle image velocimetry (PIV).

2. Technical Overview of Video Instrumentation

Modern digital imaging devices utilize a sensor known as a charge-coupled device, or CCD. The CCD is typically a single integrated circuit comprised of an array of photosensitive cells. An image is projected by a lens onto the CCD and converted to an electric charge proportional to the light intensity at each cell. Control circuitry samples the electric charge and converts it to a digital image. The digital image is essentially a two-dimensional matrix of discrete values representing the image intensity, **I**, as a function of the light intensity sampled at each cell on the CCD: $\mathbf{I} = f(u,v)$, where (u,v) represent the coordinates of the cell on the CCD. The image intensity, $\mathbf{I}_{uv}$, is a value along a monochromatic scale from black to white. For color imaging devices, a unique intensity matrix is measured for each of the three primary colors; red, green, and blue. The majority of imaging devices employ 8 bits per color channel, i.e. 256 discrete values, and thus a color gamut of approximately 16.7 million unique values.

The resolving capabilities of a digital imaging device are limited by the spatial variation and magnitude of the reflected light source, and by characteristics of the lens-camera system. Voltages induced by low light intensities $O(1\text{ lx})$ are indistinguishable from background noise induced by thermal excitation of the CCD sensor under normal operating conditions. Environmental conditions such as rain, fog, and sun glare can completely obscure the desired signal. Optical properties of the lens have a significant effect on the quality of the measured signal. A multitude of aberrations are introduced from lenses; notably spherical distortion and diffraction. Spherical distortion deforms the image as a whole, causing lines to be rendered as curves. Diffraction limits the size of

the smallest object that a lens can resolve, and is dependent on the incident wavelength. For a given lens-camera combination, the resolving capabilities are often parameterized in terms of the spatial frequency response, i.e. modulation transfer function (MTF). At frequencies where the MTF of the imaging system is 100%, there is no attenuation of features in the spatial domain.

The fields of machine vision and artificial intelligence encompass the detection and measurement of features within a digital image. Common techniques utilize mathematical and statistical representations for the occurrence and variability of values in the digital image matrix. Intuitive characteristics such as textures and features are described in terms of range, density, and gradient. Algorithms for the detection of unique features within an image often apply first derivative operators. The resulting spatial gradient accents boundaries between two dissimilar regions, and is often referred to as an edge-detector. Spatial gradients have the added effect of exaggerating noise in the image. The solution is to apply Gaussian smoothing at some stage in the process

3. Logistical Considerations for the Use of Video in the Nearshore

The nearshore environment presents certain difficulties for the application of traditional *in-situ* instruments. DICM-s, EMCM-s, ADCP-s, pressure sensors, wave gauges and resistance wires require *in-situ* installation. They are subject to fouling by biofilms, and must be capable of withstanding extreme environmental conditions. Their valuable nature also makes them susceptible to theft and vandalism, precluding their use in otherwise ideal locations.

These instruments are also limited to point measurements, or in the case of ADCP-s, a small radial field. Nearshore motions and wave fields are non-uniform alongshore (Puleo et al., 2003) and thus require a degree of spatial sampling for adequate characterization. For point-sampling instruments, this entails an array of sensors throughout the nearshore – a logistically challenging and expensive task. Temporally, their resolution may be sufficient, although record length is often constrained by the necessity of onboard data storage and battery life. In high-energy environments the data quality from these instruments may degrade. DICM-s and EMCM-s have a maximum measurable velocity; wave gauges and resistance wires are not suited for the surf zone; and ADCP-s are effectively "blinded" by foam and bubbles.

The application of video for measuring nearshore processes is a remote sensing technique relying on the measurement of electromagnetic radiation reflected from the feature of interest. As such, it shares many of the advantages and difficulties associated with remote sensing technologies. Although effective, electromagnetic radiation is only a proxy, whereas *in-situ* instrumentation are able to more closely sample the feature of interest; resulting in fewer potential sources of error.

Video is most beneficial in terms of both logistics and sampling resolutions. Video systems are low-maintenance and are relatively easy to deploy. Remote positioning prevents interference with the studied process, while simultaneously allowing for direct interfacing with data systems. By integrating with a computer network, the image acquisition software can be remotely reconfigured mid-experiment to improve data quality. As described in Section 4, each individual cell of a CCD corresponds to a sampling point. When applied to spatial measurements, the CCD represents a dense grid which effectively samples thousands of spatial points at the frequency of the device;

typically 25 Hz. Video thus has the capability to resolve most of the nearshore wave spectrum.

4. Methods

4.1 Photogrammetry

Quantification of features within photographic images requires transformation of the image to object space, i.e. real world coordinates. Conceptually, the view angle distorts the distance between features in the image relative to their true spatial distance. The transformation of features between image and spatial coordinates is accomplished using photogrammetric equations.

The following method is from *Holland et al.* (1997), using common photogrammetric equations. We define (u, v) as the 2-D coordinates of a point in an image and (x, y, z) as the 3-D spatial coordinates of the corresponding object (Figure 1). The image plane is offset from the camera optical center (x_c, y_c, z_c) by the focal length f. The view angle relates the line connecting the optical and image (u_0, v_0) centers to the spatial vertical, and is comprised of three successive rotations known as the tilt (τ), azimuth (φ), and roll (σ). The following equations allow transformations between coordinate systems:

$$\begin{aligned} u - u_0 &= -f / \lambda_u \left[\frac{m_{11}(x - x_c) + m_{12}(y - y_c) + m_{13}(z - z_c)}{m_{31}(x - x_c) + m_{32}(y - y_c) + m_{33}(z - z_c)} \right] \\ v - v_0 &= -f / \lambda_v \left[\frac{m_{21}(x - x_c) + m_{22}(y - y_c) + m_{23}(z - z_c)}{m_{31}(x - x_c) + m_{32}(y - y_c) + m_{33}(z - z_c)} \right] \end{aligned} \tag{1}$$

where λ_u and λ_v are horizontal and vertical scale factors and m_{ij} is a 3x3 matrix of rotation coefficients (Appendix A). Equations (1) are termed collinearity equations, as they describe a line transecting the camera center, image point, and object point. This system of equations, or camera model, contains eleven parameters (u_0, v_0, x_c, y_c, z_c, f, λ_u, λ_v, τ, φ, σ) and is nonlinear. *Abdel-Aziz & Karara* (1971) combined the parameters of the collinearity equations into the coefficients L_j to yield the following linear equation:

$$\begin{aligned} u &= \frac{L_1 x + L_2 y + L_3 z + L_4}{L_9 x + L_{10} y + L_{11} z + 1} \\ v &= \frac{L_5 x + L_6 y + L_7 z + L_8}{L_9 x + L_{10} y + L_{11} z + 1} \end{aligned} \tag{2}$$

The coefficients L_j are known as direct linear transformation (DLT) coefficients and are listed in Appendix A. The inverse of equations (2) is required for calculation of spatial coordinates from video imagery data:

$$\begin{bmatrix} [L_1 - L_9u][L_2 - L_{10}u][L_3 - L_{11}u] \\ [L_5 - L_9v][L_6 - L_{10}v][L_7 - L_{11}v] \end{bmatrix} \begin{bmatrix} x \\ y \\ z \end{bmatrix} = \begin{bmatrix} [u - L_4] \\ [v - L_8] \end{bmatrix} \quad (3)$$

Unfortunately equations (3) are underdetermined. In the simplest sense, a 2-D image cannot fully represent 3-D space. Constraining one of the spatial coordinates (x, y, z) yields a determined system:

(4)

$$\begin{bmatrix} x \\ y \end{bmatrix} = \frac{1}{(L_1 - L_9u)(L_6 - L_{10}v) - (L_2 - L_{10}u)(L_5 - L_9v)} \begin{bmatrix} [L_6 - L_{10}v] & [L_{10}u - L_2] \\ [L_9v - L_5] & [L_1 - L_9u] \end{bmatrix} \begin{bmatrix} [u - L_4 - z(L_3 - L_{11}u)] \\ [v - L_8 - z(L_7 - L_{11}v)] \end{bmatrix}$$

where the spatial coordinate z is now an independent variable. Thus we are able to measure real-world distances from images given one of the spatial coordinates is known. It should be noted that this is an idealized geometric relationship that neglects various error sources; notably distortion effects from the lens-camera system as noted in Section 2.

4.2 Study site

The site for this experiment was at Togcha Bay near Ipan, Guam. Togcha Bay is characterized by a shallow and uniform reef composed of macroalgae and turf overlying a pavement substrate (Figure 2). The entire nearshore section of the reef, approximately 500 m in cross-shore distance, is regularly exposed at low tide. The island of Guam was chosen because of the frequency of typhoon wave and wind driven events. The uniform profile of Ipan Reef is ideal for estimation of the effects of bathymetry and friction.

The video acquisition equipment consisted of a Sony SSC-E473 color video camera with a Fujinon 2.7 mm auto-iris lens. The equipment was installed atop an 8 m high concrete building overlooking the southern half of Togcha Bay on August 20th, 2005. Power and data signal were transferred via co-axial cable to an indoor logging computer. A Matrox Meteor II frame grabber converted the analog video to digital input. Digital input and initial pre-processing were performed using automated Matlab software. Full frame RGB images were captured in uncompressed format every 15 min. A single line of pixels spanning the image, hereafter pixel-line, was captured at 2 Hz. Data capture ran continuously (from August 20th till current) during daylight hours and was uploaded to University of Hawaii servers nightly. Timestamps were attached to each frame and pixel-line with sub-second accuracy. Timing drift was minimized by synchronizing the internal clock daily with an atomic clock via internet timeservers. The image logging system is entirely autonomous and can be reconfigured remotely.

Determination of the image to spatial coordinate system relationship, i.e. camera model calibration, followed the method of *Holland et al.* (1997). Eight permanent features within the camera field of view were chosen as ground control points (GCP) and

surveyed using a Garmin GPS receiver with a specified accuracy of ±10 m in radius. Corresponding image coordinates were then identified for each GCP (Figure 3). Surveyed GPS coordinates for the camera were used as the origin (x_c, y_c, z_c) of the spatial coordinate system. The horizontal scale factors (λ_u, λ_v), were set to unity. The rotational angles (τ, φ, σ) and the focal length (f) were estimated using an iterative nonlinear least-squares regression to equation (1), using the GCP spatial and image coordinates as predictor and response values, respectively.

Because waves are observed to break within a known, limited region, rectification to spatial coordinates is possible. Constraining the rectification of features to the surveyed x-coordinate of the reef edge creates a vertical plane (Figure 4, upper half), from which vertical measurements are subsequently made. Similarly, features shoreward of the reef edge are constrained to a vertical height corresponding to sea level, and are thus rectified to a horizontal plane (Figure 4, lower half). Both of these approximations are well suited to this experiment site, as the shallow depth of Ipan Reef ensures wave breaking and restricts waves on the reef to small-amplitude.

The spatial resolution of this method is entirely dependent on the experimental setup, i.e. geometrical relationship of the camera to the feature studied. The vertical resolution of the timestacks was 5 cm at the reef edge. To estimate the horizontal resolution, a complete spatial mapping of the individual image pixels using a constrained vertical coordinate is given in Figure 5. Pixel footprints are O(1 cm) within 100 m of the camera, and increase to O(10 m) within 500 m offshore. Because the ground control points where used for calibration of the camera model, they should not be construed as a form of experimental verification. Overall accuracy of the camera model was evaluated via comparison to a geo-referenced tagged image file with 4 m resolution (DOC, 2004) (Figure 6).

4.3 Detection Algorithm

"Timestacks" were created by concatenating the pixel-line for 600 consecutive samples, i.e. 5 min (Figure 7). After timestacks were rectified to a vertical plane, an automated image analysis algorithm was used to extract maximum breaking wave height from the video signal (Figure 8). The essential features of the detection algorithm are as follows:

1. Images are entered into the algorithm in the form of a rectified timestack. For the purposes of wave height detection, only the vertical plane is considered (subplot A, Figure 8). As described in Section 2, the image data are in the form of a $u \times t \times c$ array of image intensities, $\mathbf{I}_{utc}$, where u, t, c correspond to the spatial vertical, time, and color band intensities.
2. Remove the time mean over 5 minute periods, corresponding to the duration of a single timestack:

$$\mathbf{M}_{uic} = \mathbf{I}_{uic} - \frac{1}{N_i}\sum_{i=1} \mathbf{I}_{uic}$$

   This effectually removes features constant in time, e.g. the horizon, while emphasizing time-variant features (subplot B, Figure 8).
3. Determine the Region of Interest (ROI).

a. The image is converted to grayscale by finding the mean intensity along the three color bands:

$$\mathbf{G}_{ut} = \frac{1}{N_c}\sum_{j=1}\mathbf{M}_{utj}$$

b. The spatial gradient is calculated as:

$$\mathbf{R}_{ut} = \frac{\partial \mathbf{G}_{ut}}{\partial u}$$

c. The time-variance of the spatial gradient is then calculated:

$$\mathbf{S}_u^2 = \frac{1}{n}\sum_{i=1}^{n}(\mathbf{R}_{ui} - \overline{\mathbf{R}}_u)^2$$

d. We then calculate the spatial range of the majority of the variance in the image:

$$u_{\max} = 3 * \sqrt{\sum_{i=1}^{n}(\mathbf{S}_i^2 - \overline{\mathbf{S}})^2}$$

e. The ROI is defined as the region between the bottom of the image to $u_{\max}$, or in spatial coordinates, the region from the reef edge to the maximum vertical extent defined by $u_{\max}$. The ROI for a specific timestack is shown in subplot B, Figure 8, and corresponds to the region below the solid red line. This method uses the robust gradient to delineate where the features of interest *should* be, yet does not depend on the gradient to extract the features specifically. Identifying a unique ROI for each timestack has the advantage of adjusting to changing conditions, e.g. lighting, wave heights.

4. Extract the feature of interest, i.e. breaking waves:
   a. An iterative threshold is applied to the ROI of the full-color array **M** (subplot C, Figure 8). The intensity values of **M** are mapped to either 0 or 1 based on an initial threshold value, h, arbitrarily chosen such that $h \approx \overline{\mathbf{M}}$. We then calculate the sum of all points that lie *outside* the ROI:

$$s = \sum_{i=1}^{n}\mathbf{M}_i > h$$

   The value s is essentially a measure of the amount of noise identified, as features outside the ROI are considered background features and should ideally be mapped to 0 based on the threshold value h.
   b. The threshold value h is iteratively increased until s becomes sufficiently small. For this experiment, we found a fixed normalized value of $s = 0.01 * n_{\text{pixels}}$, where n_{pixels} is the number of points *outside* the ROI, to work well.
5. Determine breaking wave heights
   a. The algorithm then identifies the greatest, i.e. highest, value for $\mathbf{M}_t$ corresponding to each sample in time (subplot D, figure 8). Spurious points, e.g. whitecaps, noise, are discarded based on the discriminating condition that identified points must be connected to a larger body.

5. Initial Results: Wave Properties from Video Timestacks

A variety of time-dependent features are emphasized by the timestack technique. On August 30th, 2005, a low-pressure system passed the experiment site approximately 520 km to the east. The resulting wave energy provided several signals as distinguished by timestacks (Figure 7). Offshore swell is evident past the reef edge, with wave breaking limited to the abrupt interface between the reef edge and deeper water. Short-duration bores are seen for larger waves, which eventually reform into secondary swell as they propagate across the reef. Reflection from the shoreline and outward propagation is also evident.

For the estimation of breaking wave heights or similar features, four primary sources of error are identified; optical aberrations, photogrammetric error, image processing degradation, and algorithm precision. A full error analysis for each of these sources has not been completed to date. The greatest source of optical error is spherical distortion, a consequence of imperfect lenses. Holland et al. (1997) describe a camera calibration method that models, and accounts for, radial symmetric distortion using a two-coefficient odd-order polynomial. To a large degree, optical distortions can be minimized through the use of high-grade lenses. Photogrammetric error can be attributed to imprecise knowledge of the aforementioned camera model parameters (Section 4.1), with the resulting spatial measurement error specific to each setup. For this experimental setup, introduction of an angular rotation (tilt) error of $O(0.01$ rad) resulted in a Δx of $O(10$ m) at $x(500$ m). Photogrammetric errors can be reduced by the use of a large number of accurately surveyed GCPs during estimation of camera model parameters.

An often overlooked, yet significant source of error is due to degradation of the image data during processing. Many modern applications use image compression algorithms to reduce filesize, using compression techniques designed to exploit human vision system limitations. Deterioration of images due to compression can adversely affect computer based image analysis results. Ultimately, the analysis algorithm is the decisive factor for precise quantification of features from video imagery.

Time constraints limited the discussion for this paper to breaking wave heights despite the potential for measuring other processes; notably wave celerities along the reef flat and for offshore swell. A comparison between breaking wave heights measured by video is made to pressure readings from a Seabird SBE-26*plus* pressure sensor (Figure 9). The pressure sensor was located 965 m to the north of the video target, at approximately 10 m depth. A clear visual correlation exists between the two signals as offshore swell increases in height from 8.30 to 8.31, 2005. The period from 8.31 3:00-9:00 reveals occasional high breaking wave heights despite a drop in offshore swell height. This can be attributed to a low tide during this period resulting in rapid wave deformation and a powerful splash.

6. Summary and Discussion

The rapid degradation of spatial resolution with cross-shore distance from the camera creates difficulties in the measurement of horizontal features, i.e. waves, with wavelengths smaller than 10 m. The high temporal sampling used for timestacks helps offset this spatial deficit, as secondary swell can be detected in the region of poor resolution. While useful, the timestack technique removes one spatial dimension and essentially reduces the video measurements to radial distances. Resolving complete wave vectors requires a 2-dimensional subset of the image be sampled. For features measured

across the reef edge, i.e. vertical plane, the spatial and temporal resolutions are fully capable of resolving surface gravity waves and corresponding breaking heights.

Given a camera model with adequate spatial and temporal resolution, the remaining task is extraction and quantification of the feature of interest. As mentioned previously, entire fields are devoted to this task and a multitude of techniques have been developed. The ease at which a detection algorithm can be developed is largely dependent on the uniqueness of the feature of interest, e.g. color, intensity, texture, or variability. Great difficulties arise after an algorithm has been precisely tuned to work on a specific data set or subset, only to find it fails entirely for slightly different conditions. To this end, some suggestions apply. Algorithms should be relational, and require no user input or adjustment, i.e. coefficients and parameters should be expressed in terms of the image itself. This is a necessity for large time series wherein data may have low-frequency variations. As with the technique described herein, a combination of several simple techniques can be quite robust. Effectiveness at exclusively and precisely delineating the feature of interest depends on a balance of sensitivity and robustness.

Further analysis of video image data is ongoing. Future work will focus on integration of video and *in-situ* pressure sensor data for quantifying the transformation of waves across the reef, with the goal of constructing a physical representation of the complete wave energy budget as a function of tidal height, incident swell, and morphology. Such representations will be beneficial for predicting the effects of storm-induced energy in the nearshore.

REFERENCES

Aagaard, T., and J. Holm (1989), Digitization of wave run-up using video records, *J Coastal Res., 5*(3), 547-551

Abdel-Aziz, Y., and H. Karara (1971), Direct linear transformation from comparator coordinates into object space coordinates in close-range photogrammetry, *Papers from the American Society of Photogrammetry, Symposium on Close-Range Photogrammetry*, pp. 1-18, Urbana, Illinois.

Ahrens, J.P., W.N. Seelig, D.L. Ward, and W. Allsop (1993), Wave runup on and wave reflection from coastal structures. Proceedings of Ocean Wave Measurement and Analysis (Waves '93) Conference. American Society of Civil Engineers, pp. 489– 502.

Bailey, D.G., and R.D. Shand (1994), Determining wave run-up using automated video analysis. Proceedings of the second New Zealand Conference on Image and Vision Computing, pp 2.11.1-2.11.8, Palmerston North.

Department of Commerce (DOC), National Oceanic and Atmospheric Administration (2004), Guam IKONOS Mosaic Imagery 2001-2003: NOAA's Ocean Service, National Centers for Coastal Ocean Science (NCCOS), Silver Spring, MD.

Galvin, C. J (1968), Breaker type classification on three laboratory beaches, *J. Geophys. Res.*, *73*(12), 3651-3659.

Guam Benthic Habitat Maps – Biological Cover and Geomorphological Structure (2004), prepared by the National Ocean Service, Biogeography Program, in cooperation with Analytical Laboratories of Hawaii and BAE Systems Spectral Solutions

Holland, K.T., J.A. Puleo, and T.N. Kooney (2001), Quantification of swash flows using video-based particle image velocimetry, *Coast. Eng.*, *44*, 65-77.

Holland, K.T., and R.A. Holman (1999), Wavenumber-frequency structure of infragravity swash motions, *J. Geophys. Res.. 106*(C6), 13,479-13,488.

Holland, K.T., R.A., Holman, and T.C. Lippmann (1997), Practical use of video imagery in nearshore oceanographic field studies, *IEEE J. Oceanic. Eng.*, *22*(1), 81-92.

Holland, K.T., B. Raubenheimer, R.T. Guza, and R.A. Holman (1995), Runup kinematics on a natural beach, *J. Geophys. Res.*, *100*(C3), 4985-4993.

Holman, R.A., and R.T. Guza (1984), Measuring run-up on a natural beach, *Coast. Eng.*, *8*, 129-140.

Konicki, K.M., and R.A. Holman (2000), The statistics and kinematics of transverse sand bars on an open coast, *Mar. Geol.. 169*, 69-101.

Lippmann, T.C. and R.A. Holman (1991), Phase speed and angle of breaking waves measured with video techniques, in *Coastal Sediments*, edited by N. Kraus. pp. 542-556, American Society of Civil Engineering. New York.

Lippman, T.C. and R.A. Holman (1990), The spatial and temporal variability of sand bar morphology, *J. Geophys. Res.*, *95*(C7), 11,575-11,590.

Lippmann, T.C. and R.A. Holman (1989), Quantification of sand bar morphology: A video technique based on wave dissipation, *J. Geophys. Res.*, 94(C1), 995-1011.

Plant, N.G. and R.A. Holman (1997), Intertidal beach profile estimation using video images, *Mar. Geol.*, *140*, 1-24.

Puleo, J.A., G. Farquharson, S.J. Fraiser, and K.T. Holland (2003), Comparison of optical and radar measurements of surf and swash zone velocity fields, *J. Geophys. Res.*, *108*(C3), 3100-3112.

Smith, J.M (2002), Surf zone hydrodynamics, in *Coastal Engineering Manual, Part II, Hydrodynamics, Chapter II-4, Engineer Manual 1110-2-1100*, U.S. Army Corps of Engineers, Washington, DC.

Stockdon, H.F., and R.A. Holman (2000), Estimation of wave phase speed and nearshore bathymetry from video imagery, *J. Geophys. Res.*, *105*(C9), 22,015-22,033.

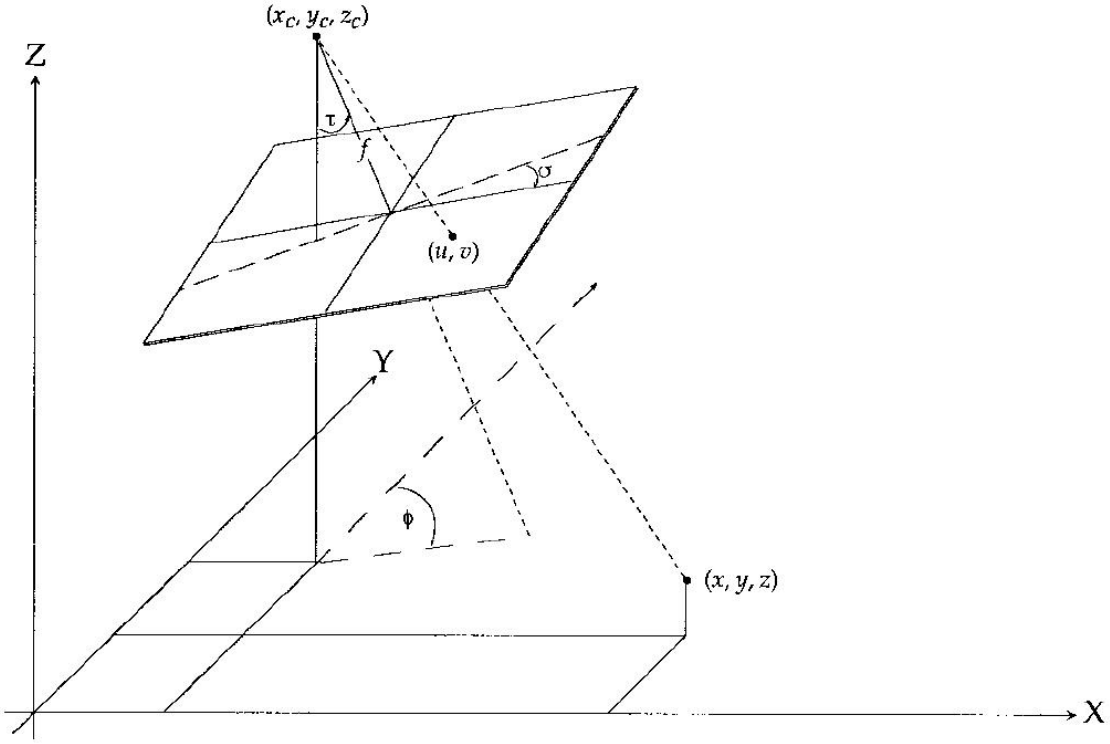

Figure 1. Relationship between image and spatial coordinate systems. A line between the camera center (x_c, y_c, z_c) and an object at point (x, y, z) creates a point (u, v) on the image plane. Knowledge of the remaining parameters for the focal length (f), and rotation angles (τ, φ, σ) allows for transformation between image and spatial coordinates. *From Holland et al. (1997).*

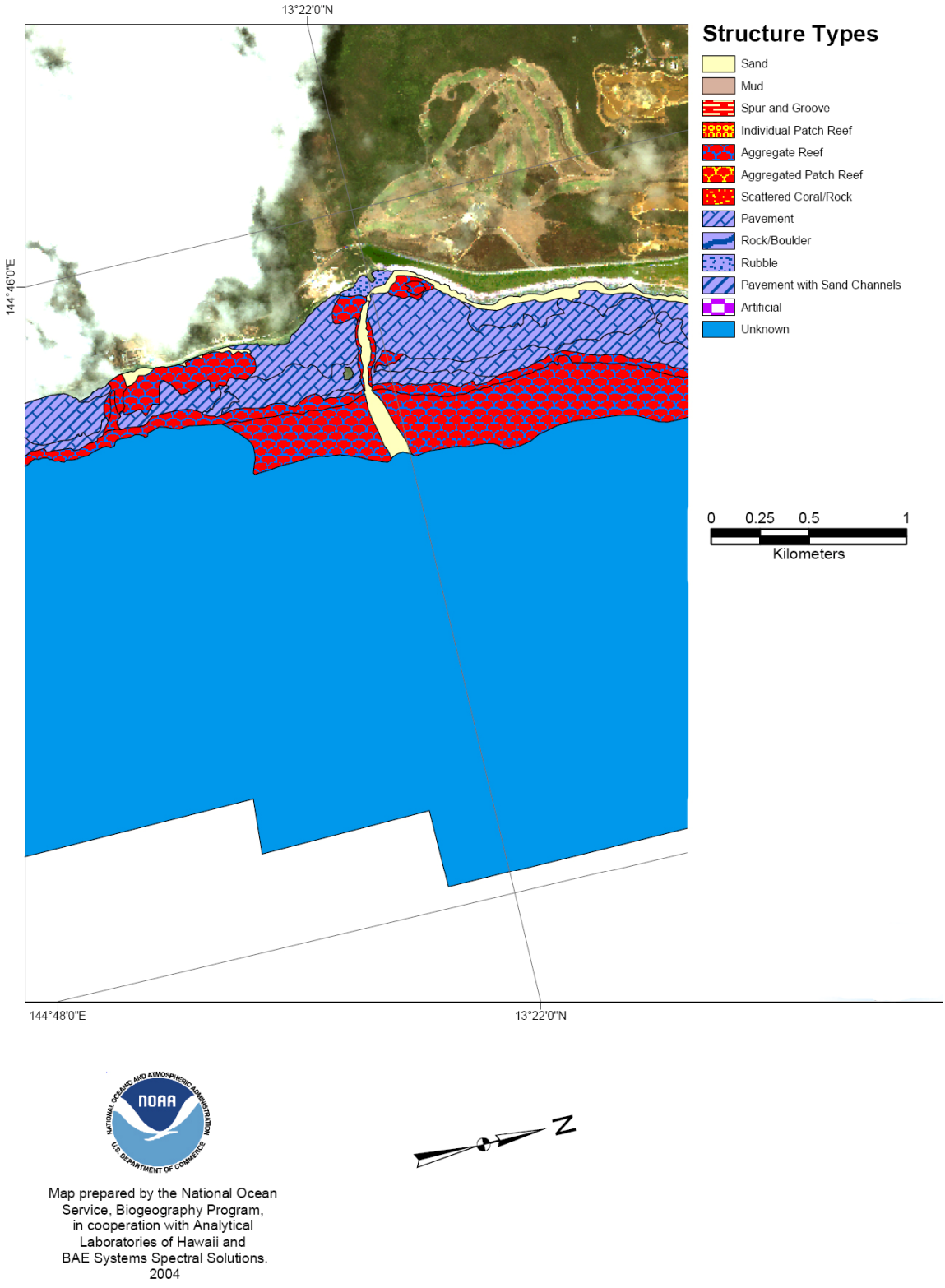

Figure 2. Geomorphological structure of Togcha Bay reef, Guam. Adapted from NOAA Guam Benthic Habitat map.

Figure 3. Surveyed ground control points (GCP-s) used in calibration of the camera model. Colored dots are corresponding image coordinates (*u, v*). Vertical black line coincides with image pixels sampled for timestacks.

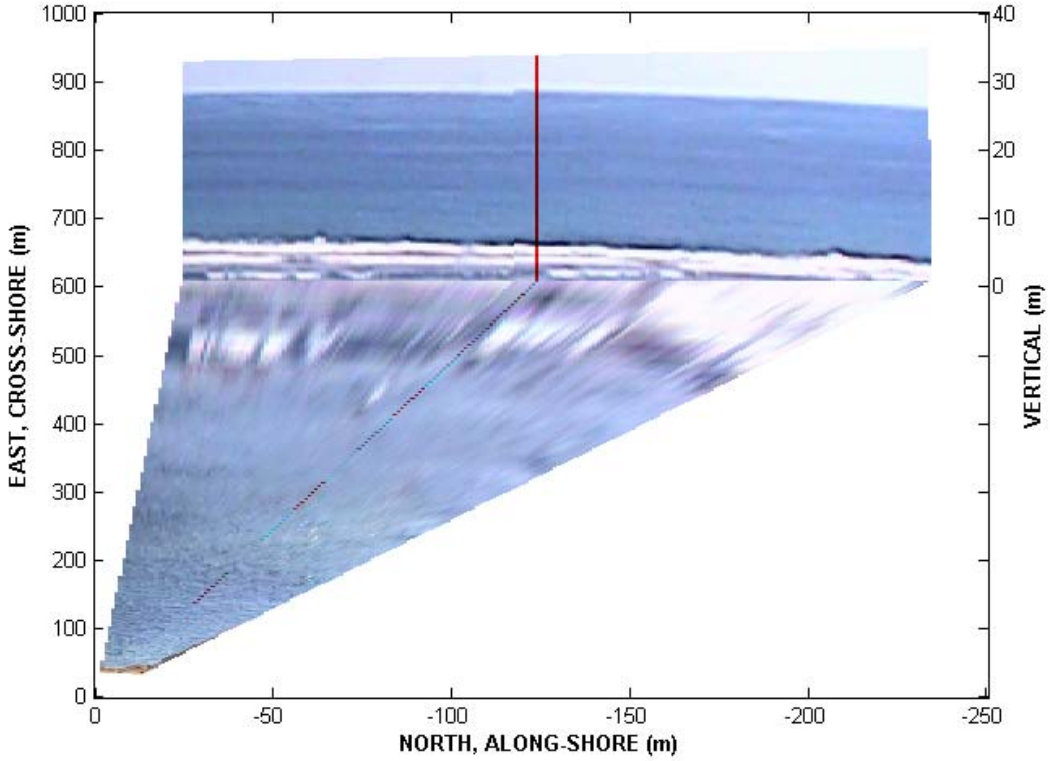

Figure 4. Rectification of image to horizontal and vertical planes. The horizontal plane extends approximately 600 m cross-shore. Note difference in vertical scale.

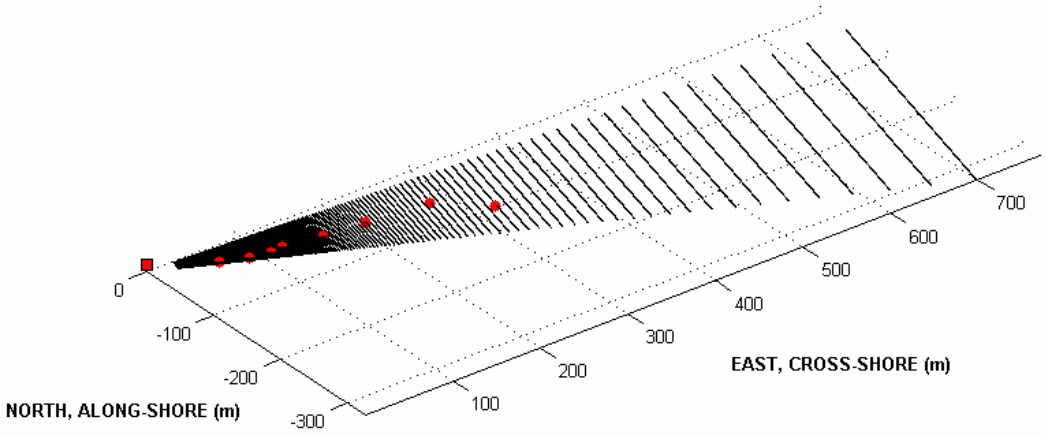

Figure 5. Spatial coordinates of ground control points (red) and image pixels (black) as calculated from equation (4) using estimated DLT coefficients. Pixel footprints are on the order of 1 cm within 100 m of the camera, and increase to order 10 m within 500 m offshore.

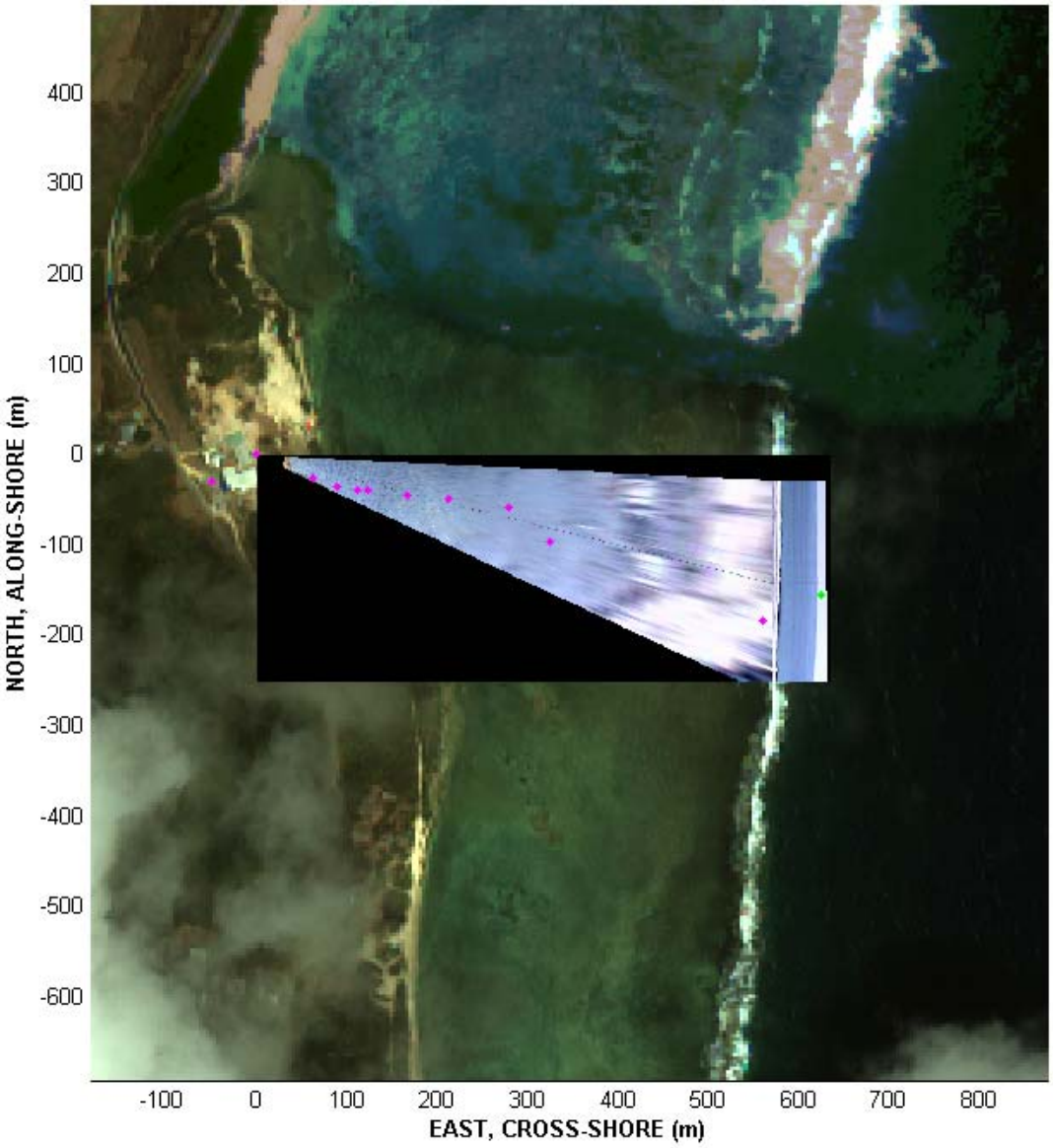

Figure 6. Comparison of camera model to geo-referenced tagged image file with 4 m resolution (DOC, 2004). The visual agreement is quite good, although a quantitative comparison has yet to be made.

Figure 7. Non-rectified timestack. Date is Aug 30th, 2005. Timespan is exactly 5 minutes. The horizontal and vertical axis corresponds to time and distance, respectively. A quantitative measurement of distance cannot be directly read from this image, as it has not yet been rectified to spatial coordinates. This figure is shown to illustrate the various features detected using video. Foremost are breaking wave heights. Bores are seen adjacent to the broken wave, eventually reforming into secondary swell as they propagate across the reef, as well as reflection from shore. Offshore swell is also evident.

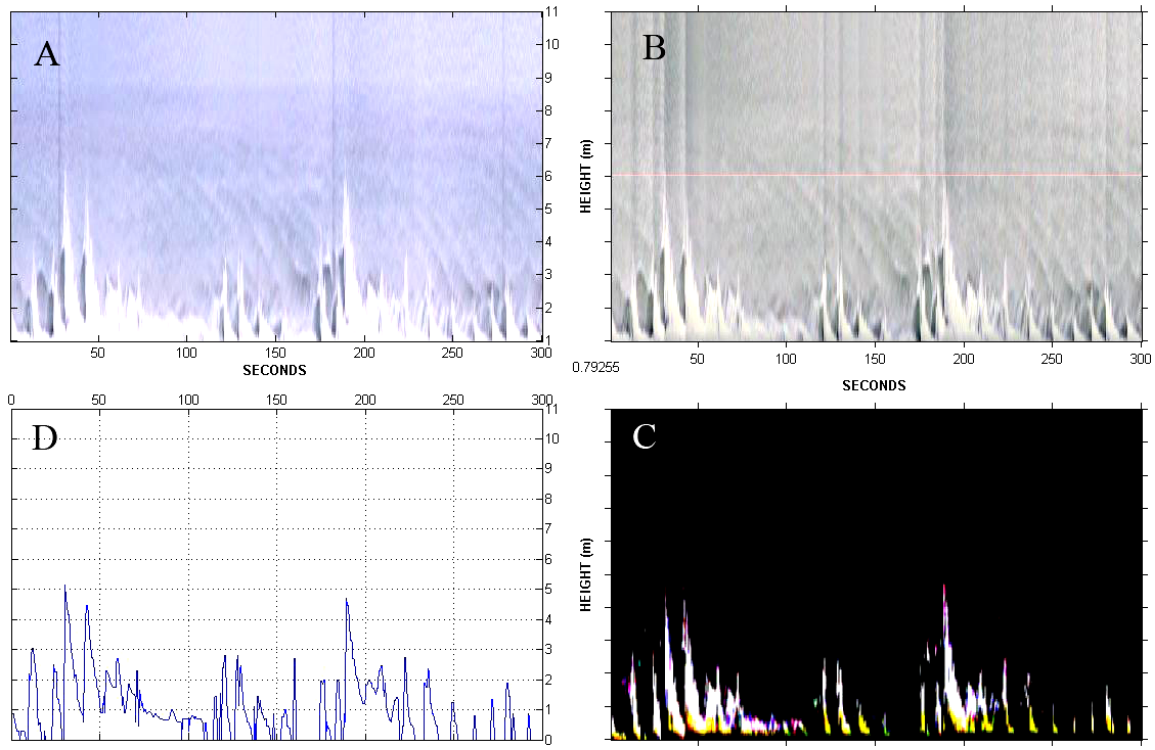

Figure 8. Wave height detection process.

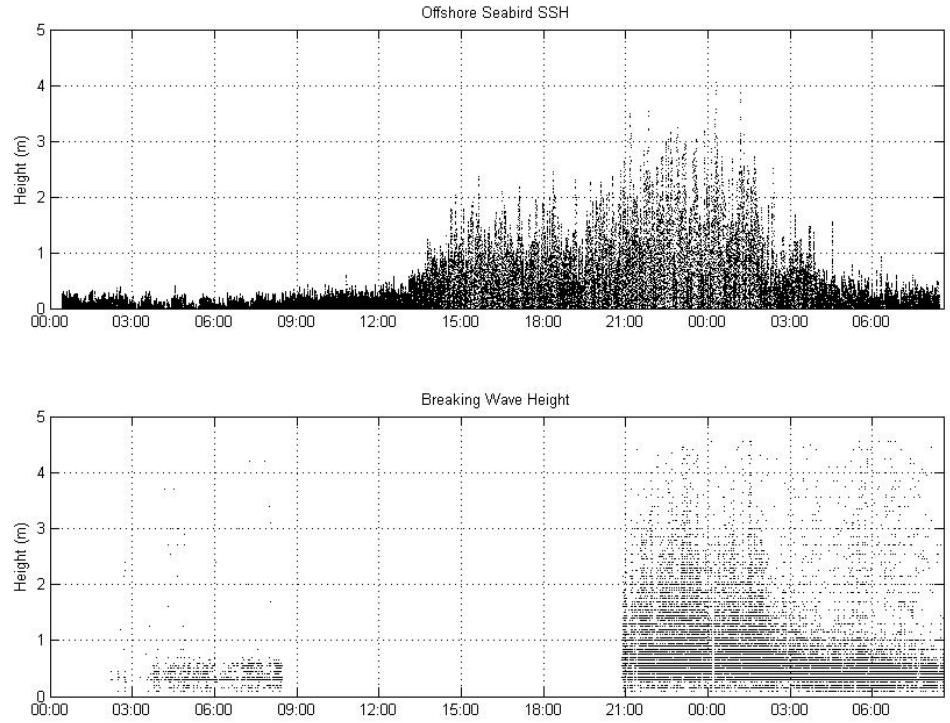

Figure 9. Comparison between video measurement and seabed-mounted pressure sensor. The pressure sensor is located 965 m to the north of the video target, at approximately 10 m depth. Times shown are for 8.30 to 8.31, 2005. Video measurements are missing for nighttime hours.

APPENDIX A

Orthogonal rotation matrix, $m_{ij,}$ from equation (1):

$$m_{11} = \cos\phi\cos\sigma + \sin\phi\cos\tau\sin\sigma$$
$$m_{12} = -\sin\phi\cos\sigma + \cos\phi\cos\tau\sin\sigma$$
$$m_{13} = \sin\tau\sin\sigma$$
$$m_{21} = -\cos\phi\sin\sigma + \sin\phi\cos\tau\cos\sigma$$
$$m_{22} = \sin\phi\sin\sigma + \cos\phi\cos\tau\cos\sigma$$
$$m_{23} = \sin\tau\cos\sigma$$
$$m_{31} = \sin\phi\sin\tau$$
$$m_{32} = \cos\phi\sin\tau$$
$$m_{33} \ -\cos\tau$$

Direct Linear Transformation (DLT) coefficients from equation (2):

$$L = (x_c m_{31} + y_c m_{32} + z_c m_{33})$$
$$L_1 = (u_0 m_{31} - f m_{11})/(\lambda_u L)$$
$$L_2 = (u_0 m_{32} - f m_{12})/(\lambda_u L)$$
$$L_3 = (u_0 m_{33} - f m_{13})/(\lambda_u L)$$
$$L_4 = -(L_1 x_c + L_2 y_c + L_3 z_c)$$
$$L_5 = (v_0 m_{31} - f m_{21})/(\lambda_v L)$$
$$L_6 = (v_0 m_{32} - f m_{22})/(\lambda_v L)$$
$$L_7 = (v_0 m_{33} - f m_{23})/(\lambda_v L)$$
$$L_8 = -(L_5 x_c + L_6 y_c + L_7 z_c)$$
$$L_9 = m_{31}/L$$
$$L_{10} = m_{32}/L$$
$$L_{11} = m_{33}/L$$

Analogous form of equation (4), where the spatial coordinate x, has been constrained:

$$\begin{bmatrix} y \\ z \end{bmatrix} =$$
$$\frac{1}{(L_2 - L_{10}u)(L_7 - L_{11}v) - (L_3 - L_{11}u)(L_6 - L_{10}v)} \begin{bmatrix} [L_7 - L_{11}v] & [L_{11}u - L_3] \\ [L_{10}v - L_6] & [L_2 - L_{10}u] \end{bmatrix} \begin{bmatrix} [u - L_4 - x(L_1 - L_9 u)] \\ [v - L_8 - x(L_5 - L_9 v)] \end{bmatrix}$$